Journal of Energy Storage 132 (2025) 117957

Contents lists available at ScienceDirect

Journal of Energy Storage

journal homepage: www.elsevier.com/locate/est

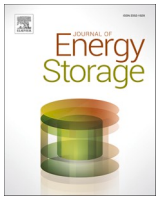

Research papers

Revealing the potential of double perovskite hydrides A_2SiH_6 (A = Li and Na) for solid-state hydrogen storage applications

Abdullah Candan [a,*], Aytac Erkisi [b], Bugra Yildiz [c]

[a] Department of Machinery and Metal Technology, Kirsehir Ahi Evran University, Kirsehir 40100, Turkey
[b] Computational and Gravitational Physics Laboratory, Department of Physics, Pamukkale University, Denizli 20020, Turkey
[c] Department of Physics Engineering, Hacettepe University, Ankara 06800, Turkey

ARTICLE INFO

Keywords:
DFT
Hydrogen storage
Double perovskites
HSE06
Desorption temperatures

ABSTRACT

Hydrogen's potential as a clean energy source has made hydrogen storage a critical focus of modern research. Among candidate materials, advanced double perovskite hydrides have emerged as promising options for hydrogen storage applications due to their structural versatility and favorable physical properties. In this study, a comprehensive first-principles analysis was conducted to investigate the structural, mechanical, electronic, and hydrogen storage characteristics of A_2SiH_6 (A = Li and Na) double perovskite-type hydrides. The calculated tolerance factors indicate that both hydrides possess stable cubic perovskite structures, while their negative enthalpy of formation further validates their thermodynamic stability. Moreover, the AIMD simulations were performed to investigate the thermal stability of these compounds. Electronic band structure calculations revealed that both Li_2SiH_6 and Na_2SiH_6 exhibit semiconducting behavior, with indirect band gaps calculated as 1.28 eV and 1.44 eV using GGA-PBE, and 2.22 eV and 2.32 eV using the more accurate HSE06 functional, respectively. Moreover, their mechanical stability is confirmed by compliance with Born's criteria, suggesting their robustness under operational conditions. In addition to these properties, hydrogen storage capacity evaluations demonstrated significant gravimetric hydrogen contents of 12.60 wt% for Li_2SiH_6 and 7.55 wt% for Na_2SiH_6, indicating their potential as high-capacity hydrogen storage materials. Furthermore, dielectric constant, refractive index, and absorption coefficient calculations were performed to fully characterize their electronic behavior. Overall, these results suggest that A_2SiH_6 (A = Li and Na) hydrides are promising candidates for hydrogen storage applications, supported by their favorable tolerance factors, structural stability, electronic properties, and thermodynamic features.

1. Introduction

The rapid pace of industrialization has triggered a global energy crisis. While fossil fuels have long satisfied humanity's energy demands, their reserves are now rapidly depleting. Moreover, fossil fuel consumption is a leading cause of environmental pollution and climate change [1–3]. Consequently, it is imperative to identify cleaner and renewable energy sources, prompting extensive scientific research in this field [4–8].

Hydrogen has emerged as a viable alternative energy carrier due to its abundance, low density, and clean combustion properties [9]. Recent investigations into double perovskite hydrides reveal that they offer remarkable potential for solid-state hydrogen storage applications. In addition to perovskite-based systems, recent review studies have emphasized that hydrogen storage remains a significant bottleneck for the widespread deployment of hydrogen energy technologies, highlighting the need for safe, efficient, and cost-effective storage solutions [10,11]. Various hydrogen storage technologies, including compressed gas, liquefied hydrogen, underground storage, and material-based solid-state storage, have been extensively studied, each with unique advantages and limitations [12–14]. Among these, solid-state storage methods, particularly metal hydrides, complex hydrides, and perovskite-type hydrides, have attracted increasing attention due to their high volumetric and gravimetric capacities as well as favorable thermodynamic and kinetic properties [15].

Building upon these findings, numerous recent studies have focused on advancing hydrogen storage technologies through innovative material designs and catalytic strategies [16–18]. Recent studies have

* Corresponding author.
E-mail address: acandan@ahievran.edu.tr (A. Candan).

https://doi.org/10.1016/j.est.2025.117957
Received 10 March 2025; Received in revised form 10 July 2025; Accepted 2 August 2025
Available online 6 August 2025

reported significant advances in hydrogen storage materials and their catalytic and phase transition behaviors. These include Co–Fe–B@g–C_3N_4 thin film catalysts for $NaBH_4$ hydrolysis [16], noble metal/2D MOF heterostructures for MgH_2 hydrogen storage enhancement [17], and phase transition mechanisms in Zr_2Co–H systems [18]. These examples further demonstrate the diversity of approaches for efficient hydrogen storage applications.

Hydrogen's combustion produces only water and no greenhouse gases, giving it a significant advantage as a preferred energy carrier. Furthermore, burning hydrogen releases nearly three times more energy than liquid fuels like gasoline. Currently, various methods are employed to produce hydrogen. One of the simplest ways is decomposing hydrogen-containing compounds, such as organic acids [19] and hydrocarbons [20,21]. However, water remains the most cost-effective and favored source of hydrogen, especially because wastewater and seawater can be utilized.

In addition to these advantages, double perovskite (DP) materials have recently attracted significant attention for their structural versatility and wide-ranging energy applications. These include proton conduction, ferroelectrics, battery materials, electrocatalysis, photovoltaics, optoelectronics, and thermoelectric devices [22–27]. Recent density functional theory (DFT) studies have systematically investigated a wide range of double perovskite compounds, such as Ba_2AlTMO_6 (TM = W, Re, Os) [24], Cs_2XBeBr_6 (X = Ge, Sn) [25], and various $Cs_2B'B''X_6$ halide perovskites [26,27], highlighting their promising electronic, optical, thermoelectric, and multifunctional energy properties. These works emphasize the importance of understanding the comprehensive physical properties of perovskite-type materials to guide their application in sustainable and clean energy technologies.

The alkali metal A–Si–H systems (A = Li, Na, and K) have garnered considerable interest due to theoretical predictions indicating the presence of hydrogen-rich ternary phases at high pressures. These phases may exhibit superionic, superconducting, and hydrogen storage characteristics [28–32]. These estimations indicate that at lower pressures (up to 50 GPa), A–Si–H systems often exhibit a stable compound, A_2SiH_6, characterized by octahedral SiH_6^{-2} species in which silicon achieves a hypervalent bonding configuration. Liang et al. [29] proposed Na_2SiH_6 as a H^- superionic conductor in the pressure range of 4 to 10 GPa at temperatures around 1000 °C. Another study by Xie et al. [31] attributed advantageous hydrogen storage properties to K_2SiH_6. In two studies conducted by Liang et al. and Xie et al., it was reported that compounds such as $KSiH_8$, K_2SiH_8, $KSiH_7$, Na_3SiH_{10}, and Na_2SiH_{14} become stable with structures where octahedral units are bonded and H_2 molecules are additionally included at various high pressures between 50 and 200 GPa. In addition, Liang et al. revealed that compounds such as $LiSiH_6$, Li_2SiH_{10}, $LiSiH_5$, Li_2SiH_{12}, and Li_3SiH_{10} from Li–Si–H systems are more stable at high pressures and have a high hydrogen storage capacity [28]. $LiSiH_8$ and $LiSi_2H_9$ are anticipated to exhibit favorable phonon-mediated superconductivity at pressures over 170 GPa. Notwithstanding the intriguing outcomes from computational structure prediction, so far, only the polymorphism K_2SiH_6 has been documented from experimental high-pressure studies [33]. This molecule remains stable at atmospheric pressure, adopting the cubic K_2PtCl_6 structure [34].

Discovering and examining new materials for hydrogen storage has become increasingly important, since hydrogen is considered a clean and low-cost energy source. In this context, the present computational study using density functional theory (DFT) investigates the structural, mechanical, optoelectronic, and hydrogen storage properties of alkali metal A–Si–H hydrides. The findings regarding these physical properties are remarkable, suggesting that the studied hydrides are suitable candidates for hydrogen storage and optoelectronic applications due to their semiconductor characteristics. In particular, optical absorption calculations were performed to evaluate the electronic transitions and band gap behavior of these materials, which is crucial for understanding their potential use in photocatalytic-assisted hydrogen release and other multifunctional energy applications.

Importantly, to the best of our knowledge, this is the first comprehensive study that systematically investigates Li_2SiH_6 and Na_2SiH_6 double perovskite-type hydrides under ambient conditions for their solid-state hydrogen storage capabilities. Previous studies have primarily focused on their high-pressure stability or superionic behavior [28–30,32]. In contrast, our work uniquely combines structural, electronic (including hybrid functional HSE06), mechanical, optical, and dynamic (phonon and AIMD) analyses within a single investigation. This holistic approach establishes a foundational understanding of these materials and fills a critical gap in literature, contributing new insights for their practical use in hydrogen storage applications.

2. Methodology

This study employs computations using the VASP (Vienna Ab initio Simulation Package) software [35–37], where the projector-augmented-wave (PAW) method [38] is applied to model electron-ion interactions. The total energies of both compounds remained almost constant with plane-wave energy cut-offs ranging from 400 eV to 1000 eV and k-point grids from 8 to 16. Based on these tests, the plane-wave cut-off energy was set to 554 eV for Li_2SiH_6 and 717 eV for Na_2SiH_6, while a 12 × 12 × 12 Monkhorst-Pack k-point grid [39] was used for both compounds in all subsequent structural, electronic, and optical property calculations to ensure accuracy and reliability. Furthermore, the interactions among electrons have been characterized by using pseudopotentials of the Perdew, Burke, and Ernzerhof (PBE) type within the context of the generalized gradient approximation (GGA) [40]. Since the GGA-PBE method usually underestimates the band gap of materials, a more precise exchange-correlation functional, the Heyd-Scuseria-Ernzerhof (HSE06) functional was used to explore the optoelectronic properties of A_2SiH_6 (A = Li and Na) double perovskite hydrides [41]. The relaxation operations for the related compositions have been carried out until all forces and pressures are reduced to negligible levels. After 10 optimization steps, relaxation energy was reached for Li_2SiH_6, while for Na_2SiH_6, it was reached after 23 optimization steps. In the geometric optimizations of this study, the energy-convergence criterion was established at 10^{-8} eV/atom. Additionally, the Li, Na, Si, and H atoms in the relevant compositions were taken into account with the valence configurations of $1s^22s^1$, $2p^63s^1$, $3s^23p^2$, and $1s^1$, respectively. Vesta software has been used to calculate the electron density distributions [42]. Directional dependencies of mechanical properties were determined using the VELAS code, an open-source toolbox for visualization and analysis of elastic anisotropy [43]. The stress-strain method [44], as applied in VASP, has been utilized to acquire elastic constants. Ab initio molecular dynamics (AIMD) simulations were conducted to evaluate the thermal stability of the structures at room temperature (300*K*). The phonon spectrum was calculated using the Phonopy package to assess the dynamic stability of A_2SiH_6 (A = Li and Na) [45,46].

3. Results and discussions

In this section, we present the structural, mechanical, electronic, and optical features of A_2SiH_6 (A = Li and Na) double perovskite hydrides, which are investigated using density functional theory (DFT) calculations. These hydrides unveil potential for hydrogen storage applications due to their favorable stability, mechanical resilience, and promising optoelectronic characteristics. The results are examined in the following subsections.

3.1. Structural and hydrogen storage properties

The structural features of A_2SiH_6 (A = Li and Na) double perovskite hydrides have been explored through first-principles calculations. The chemical representation of these materials, which are members of the

perovskite family, is A_2BH_6 double perovskite. These hydrides crystallize in the cubic K_2PtCl_6 structure with space number 225 (*Fm-3m*) [47]. The optimized crystal structures of A_2SiH_6 (A = Li and Na) are presented in Fig. 1, to visualize the atomic arrangements. The A atoms (8c) are located at (0, 0.25, 0.25), Si atoms (4a) at (0, 0, 0), and H atoms (24e) at (x_H, 0, 0) in the unit cell. Specifically, x_H represents the internal coordinate of hydrogen atoms within the cubic perovskite lattice, determining their fractional position along the crystallographic axes in Wyckoff sites. The total energy-volume relationship has been analyzed to evaluate the equilibrium states of Li_2SiH_6 and Na_2SiH_6. The energy-volume plots for A_2SiH_6 (A = Li and Na) perovskites have been presented in Fig. 2(a) and (b), respectively. The optimized total energy curves indicate that Na_2SiH_6 displays a slightly larger equilibrium volume and energy than Li_2SiH_6, this finding is coherent with its greater lattice parameter. The calculated lattice constant (a_0), Bulk modulus (B), pressure derivative of the Bulk modulus (B'), tolerance factor (t_G), and formation enthalpy (ΔH_f) have been given in Table 1. The lattice constants of Li_2SiH_6 and Na_2SiH_6 have been determined as 6.561 Å and 7.027 Å, respectively, indicating an increase with increasing atomic size of A-site cations. The calculated structural parameters for Na_2SiH_6 (lattice constant a_o = 7.027 Å, volume V = 362.223 Å^3, x_H = 0.2289) are in good agreement with the values reported in the OQMD crystal database [48]. Furthermore, Li_2SiH_6 exhibits greater stiffness than Na_2SiH_6 hydride as a result of its elevated Bulk modulus. Our findings exceed the documented values for K_2SiH_6 (18.33 GPa) [47], Rb_2SiH_6 (16.63 GPa) [47], Na_2PtH_6 (22.626 GPa) [49] and K_2GeH_6 [50].

The tolerance factors (t_G) for both compounds are within the stability range of perovskite structures, hence affirming the structural viability of A_2SiH_6 materials [51]. Our research reveals that the tolerance factors for the materials, particularly Na_2SiH_6 hydride, are about 1, indicating a nearly perfect cubic perovskite structure and implying significant structural stability. The negative formation enthalpies (ΔH_f) can be expressed as follows [50] suggesting that these compounds are thermodynamically stable, with sodium-containing materials exhibiting marginally superior stability compared to lithium-containing materials.

$$\Delta H_f = [(E(A_2SiH_6) - (2E_A + E_{Si} + 6E_H))]/9 \quad (1)$$

The calculated formation enthalpy for Li_2SiH_6 was found to be −0.0730 eV/atom, while for Na_2SiH_6 it was −0.0839 eV/atom, which is in good agreement with the value of −0.0840 eV/atom reported in the OQMD crystal database [48]. This comparison validates the reliability of our computational methodology and supports the energetic stability of these hydrides.

Additionally, X-ray diffraction (XRD) patterns have been produced to verify the crystalline characteristics of the optimal configurations of A_2SiH_6 (A = Li and Na). The XRD spectra of Li_2SiH_6 and Na_2SiH_6 are illustrated in Fig. 1(a) and (b), displaying the distinctive diffraction peaks of these perovskite hydrides. The principal diffraction peak for Li_2SiH_6 is located at 21.58°, whereas the strong peak for Na_2SiH_6 is seen at 37.42°. Furthermore, Na_2SiH_6 has a greater lattice parameter (7.027 Å) than Li_2SiH_6 (6.561 Å), as seen in Table 1. The observed diffraction patterns validate the structural integrity of both crystals and correspond accurately to the cubic perovskite symmetry [52]. The XRD spectra validates the viability of manufacturing these compounds while maintaining their cubic perovskite phase. These structural insights establish a foundation for assessing the mechanical, electronic, and hydrogen storage characteristics of A_2SiH_6 double perovskite hydrides in the next sections.

The evaluation of the gravimetric density of hydrogen plays a critical role in determining the efficiency and capacity of hydrogen storage. In

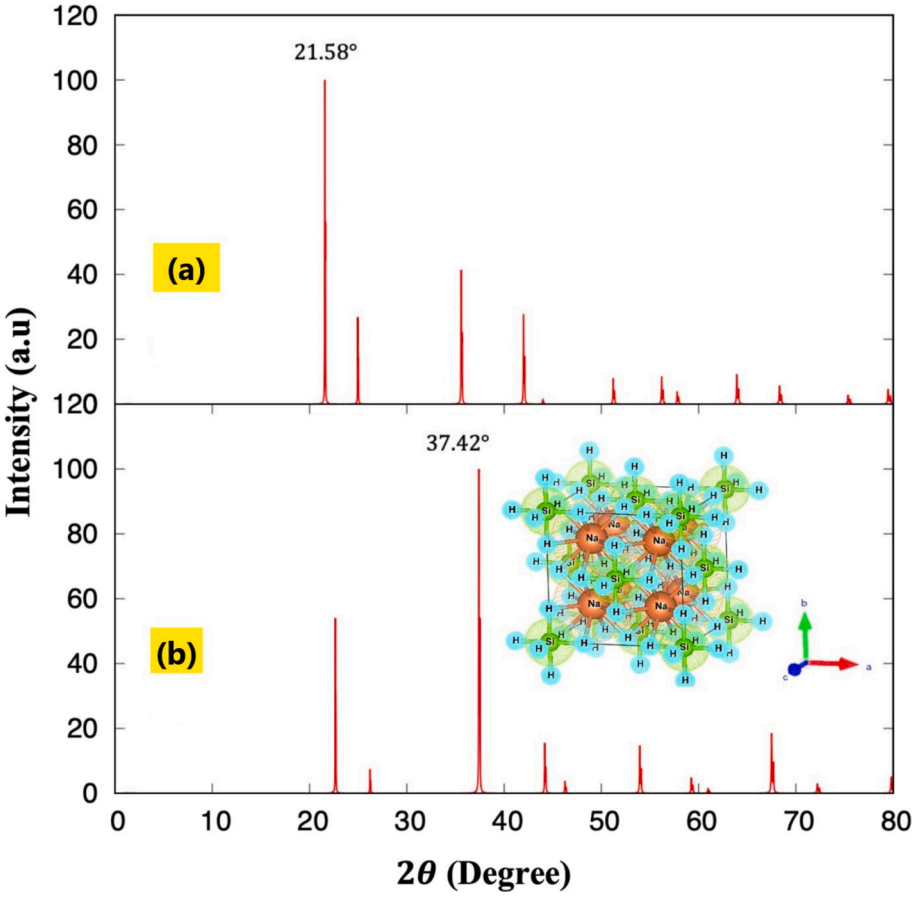

Fig. 1. The X-ray diffraction (XRD) pattern of (a) Li_2SiH_6 and (b) Na_2SiH_6 perovskite hydrides.

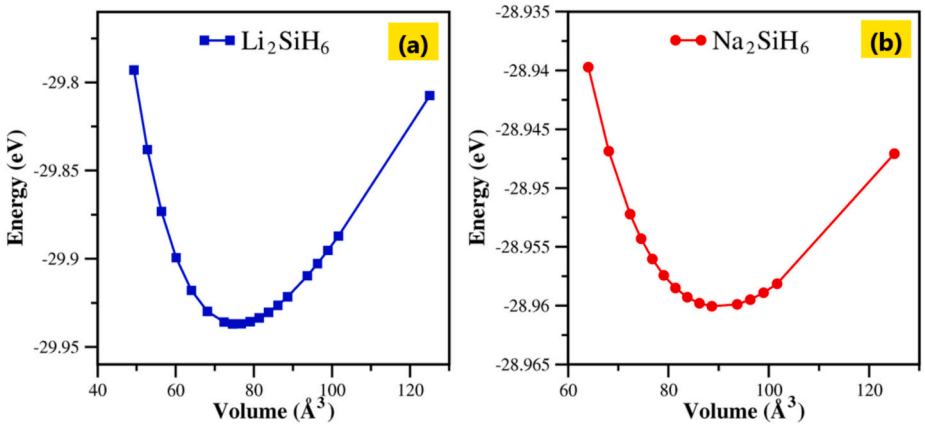

Fig. 2. The optimized total energy-volume curve for (a) Li_2SiH_6 and (b) Na_2SiH_6.

Table 1
The calculated lattice constant (a_0), Bulk modulus (B), pressure derivative of the Bulk modulus (B'), unit cell volume (V), tolerance factor (t_G), and formation enthalpy (ΔH_f) for A_2SiH_6 (A = Li and Na) hydrides.

Material	Ref.	α_0 (Å)	B (GPa)	B'	V	x_H	t_G	ΔH_f (eV/atom)
Li_2SiH_6	This work	6.561	31.20	3.53	282.359	0.2444	0.87	−0.0730
Na_2SiH_6	This work	7.027	25.60	3.67	362.223	0.2289	0.98	−0.0839
	[48]	6.881	–	–	325.84	0.2333	–	−0.0840
K_2SiH_6	[31]	7.867	20.58	4.03	480.520	0.205	–	–
K_2SiH_6	[47]	7.855	18.33	–	484.664	0.206	–	–
Rb_2SiH_6	[47]	8.204	16.63	–	552.210	–	–	–
K_2GeH_6	[50]	7.968	14.94	–	505.991	0.213	–	–
K_2SnH_6	[50]	8.338	9.91	–	579.679	0.226	–	–

this study, our focus is on the gravimetric density of hydrogenated double perovskite-type material [53]. The following equation was used to determine the hydrogen storage capacity of A_2SiH_6 (A = Li and Na) double perovskites [54]:

$$C_{wt}(\%) = \left(\frac{nM_H}{M_{host} + nM_H}\right) \times 100 \quad (2)$$

Here, n represents the atomic ratio of hydrogen to the parent compound (H/M), M_H represents the molar mass of hydrogen, and M_{host} represents the molar mass of the parent compound. The details of the gravimetric density analysis performed in our study are presented in Table 2, where the results are comparatively reported alongside other hydride materials. As a result of the calculations, the gravimetric density was found to be 12.60 wt% for Li_2SiH_6 and 7.55 wt% for Na_2SiH_6. These gravimetric capacity values are relatively high, indicating that A_2SiH_6 (A = Li and Na) is a promising material for hydrogen storage applications.

Volumetric storage capacity denotes the quantity of hydrogen contained inside a certain volume. The potential for hydrogen storage may be quantified in terms of volume, as shown in Ref. [55]:

$$\rho_{vol} = \frac{N_H \times m_H}{V\,(L) \times N_A} \quad (3)$$

where N_H denotes the number of absorbed hydrogen atoms, m_H signifies the molecular mass of hydrogen, $V\,(L)$ indicates the volume of the absorber, and N_A represents Avogadro's number. The calculated volumetric hydrogen storage capacity values (ρ_{vol}) are shown in Table 2. The Li_2SiH_6 compound exhibits superior volumetric density relative to the Na_2SiH_6 hydride owing to its reduced unit cell volume.

Compounds with exceptional properties for storing hydrogen should have high storage density and a suitable hydrogen release temperature. One of the important factors to be considered in this context is the desorption temperature (T_{des}), which can be determined using the Gibbs relationship.

$$\Delta G = \Delta H - T_{des}.\Delta S \quad (4)$$

Under standard conditions, when the change in Gibbs free energy (ΔG) at a given temperature and pressure is equal to zero, the desired desorption temperature (T_{des}) can be calculated using the relevant equation [56].

$$T_{des} = \frac{|\Delta H|}{\Delta S} \quad (5)$$

Previous experiments have shown that the entropy change (ΔS) of hydrogen is 130.7 J/mol K [57]. The ideal desorption temperature range is generally accepted as 233–333 K [58]. As shown in Table 2, the calculated T_{des} values for Li_2SiH_6 and Na_2SiH_6 are 107.78 K and 123.88 K, respectively. Although these values are below the target range of 233–333 K established by the US Department of Energy for hydrogen storage systems by 2025 [59], they indicate that hydrogen can be released at relatively low temperatures, which may be advantageous for certain cryogenic or low-temperature storage applications.

As summarized in Table 2, the hydrogen storage performance of

Table 2
The gravimetric (C_{wt}) and volumetric (ρ_{vol}) hydrogen storage capacity, and desorption temperatures (T_{des}) of A_2SiH_6 (A = Li and Na) hydrides.

Material	C_{wt} (%)	ρ_{vol} (g·H_2/L)	ΔH (KJ/mol·H_2)	T_{des} (K)	Reference
Li_2SiH_6	12.60	142.25	−14.08	107.78	This work
Na_2SiH_6	7.55	115.74	−16.18	123.88	This work
K_2SiH_6	5.2	–	–	–	[47]
Rb_2SiH_6	2.86	–	–	–	[47]
K_2GeH_6	3.84	–	–	719.3	[50]
K_2SnH_6	2.97	–	–	221.1	[50]
Mg_2CrH_6	5.60	150.05	–	230.35	[54]
Mg_2MnH_6	5.51	142.07	–	208.65	[54]

A_2SiH_6 double perovskite hydrides was comparatively evaluated against similar hydrides with the same crystal structure, considering their gravimetric and volumetric storage capacities as well as hydrogen desorption temperatures.

Li_2SiH_6 shows a volumetric hydrogen storage capacity of 142.25 g H_2/L, which is comparable to Mg_2MnH_6 (142.07 g H_2/L) and slightly lower than Mg_2CrH_6 (150.05 g.H_2/L) [54]. Moreover, its gravimetric capacity is 12.60 wt%, significantly higher than that of Mg_2CrH_6 (5.60 wt%) and Mg_2MnH_6 (5.51 wt%) [54]. Additionally, the desorption temperature of Li_2SiH_6 (107.78 K) is much lower than Mg-based complex hydrides such as Mg_2CrH_6 (230.35 K) and Mg_2MnH_6 (208.65 K), indicating favorable hydrogen release [54].

On the other hand, Na_2SiH_6 exhibits a volumetric hydrogen storage capacity of 115.74 g.H_2/L, slightly lower than Li_2SiH_6 but still competitive among reported hydrides. Its gravimetric capacity (7.55 wt %) is lower than Li_2SiH_6 but higher than K_2SiH_6 (5.2 wt%), Rb_2SiH_6 (2.86 wt%) [47] and Mg_2MnH_6 (5.51 wt%) [54]. Furthermore, the desorption temperature of Na_2SiH_6 (123.88 K) is substantially lower than those of Mg_2CrH_6 and Mg_2MnH_6, suggesting relatively easier hydrogen desorption [54].

Overall, these comparative results clearly demonstrate that Li_2SiH_6 and Na_2SiH_6 exhibit competitive volumetric hydrogen storage capacities, with Li_2SiH_6 particularly outperforming many complex hydrides due to its superior combination of gravimetric and volumetric capacities alongside low desorption temperatures. These findings highlight their promising potential as solid-state hydrogen storage materials suitable for practical energy applications.

3.2. Elastic properties and mechanical stability

Elastic features and mechanical stability are critical for evaluating a material's ability to withstand applied loads and preserve its structural integrity [60]. Their mechanical properties determine the strength against applied loads and the longevity of perovskite materials under varying operating circumstances. Higher elastic moduli signify increased stiffness and resistance to deformation, hence diminishing the likelihood of structural damage. These properties are essential for electronic device construction. Moreover, materials exhibiting ductility and anisotropy offer enduring resilience and flexibility, rendering them ideal for the fabrication of resilient electronics [61]. The assessment of mechanical stability, bonding interactions, flexibility, and thermodynamic characteristics, including melting point, specific heat, and Debye temperature, is contingent upon elastic constants [62]. In this study, the elastic constants C_{ij} (C_{11}, C_{12}, and C_{44}) were determined by studying the stress-strain relationship [63]. The elastic stability of materials is evaluated by the Born stability criterion [64,65].

$$C_{11} - C_{12} > 0, C_{11} + 2C_{12} > 0, C_{11} > 0, C_{44} > 0 \tag{6}$$

Consequently, the examined materials conform to the Born stability criterion, as shown in Table 3. A_2SiH_6 (A = Li and Na) double perovskite hydrides have been determined to be mechanically stable. On the other hand, Cauchy pressure (C_P) is also an important mechanical parameter that provides information about the ductility or brittleness of a material. It is defined using elastic constants as follows:

$$C_P = C_{12} - C_{44} \tag{7}$$

The negative (positive) sign of the C_P parameter indicates the brittle (ductile) nature of a material [66]. The computed C_P values for these hydrides are shown in Table 3. The positive results for these hydrides confirm their ductility.

Furthermore, these elastic constants allow the examination of various mechanical parameters such as Bulk modulus (B), Shear modulus (G), Young's modulus (E), B/G, and Poisson's ratio (ν) using the Voigt, Reuss, and Hill approximations [67–69]. The mechanical parameters were computed using the following equations [70] for the A_2SiH_6 (A = Li and Na) double perovskites, and the obtained values are given in Table 4.

$$B = \frac{(2C_{12} + C_{11})}{3} \tag{8}$$

$$G_V = \frac{1}{5}(3C_{44} - C_{12} + C_{11}) \tag{9}$$

$$G_R = \frac{(C_{11} - C_{12})5C_{44}}{4C_{44} + 3(C_{11} - C_{12})} \tag{10}$$

$$G_H = G = \frac{1}{2}(G_V + G_R) \tag{11}$$

$$E = \frac{9BG}{G + 3B} \tag{12}$$

The results demonstrate that Na_2SiH_6 is stiffer than Li_2SiH_6 owing to higher values of Bulk modulus (B), Shear modulus (G), and Young's modulus (E). Additionally, Poisson's ratio (ν) quantifies the bonding characteristics of materials and may be determined using the following equation [71]:

$$\nu = \frac{3B - 2G}{2G + 6B} \tag{13}$$

Poisson's ratio of 0.1 signifies covalent bonding, but a ν value of around 0.25 is indicative of ionic bonding features in materials [72]. The ionic characteristics of A_2SiH_6 (A = Li and Na) double perovskites align well with the previously published findings on K_2SiH_6 [47], Rb_2SiH_6 [47], A_2OsH_6 (A = Ca, Ba, Mg, and Sr) [73], and A_2PtH_6 (A = K, Rb) [74].

Nonetheless, Pugh's G/B ratio also dictates the bonding characteristics of the material, with a G/B ratio of around 1.1 (0.6), indicating covalent (ionic) bonding [70]. The results indicated that the existing materials had an ionic bonding nature, consistent with Poisson's ratio findings.

Additionally, one can classify the material as ductile or brittle by examining Pugh's ratio (B/G). If Pugh's B/G value exceeds (falls below) 1.75, it indicates the material exhibits ductile (brittle) behavior [75,76]. Table 4 demonstrates that A_2SiH_6 (A = Li and Na) hydrides exhibit ductile behavior, similar to other reported materials known for their ductility, such as Mg_2OsH_6 (1.79) [73], Ca_2OsH_6 (1.80) [73], Mg_2CrH_6 (2.32) [54], and Mg_2MnH_6 (1.97) [54]. The positive C_P values (6.73 GPa for Li_2SiH_6 and 5.95 GPa for Na_2SiH_6) together with B/G ratios exceeding 1.75 (2.25 for Li_2SiH_6 and 2.09 for Na_2SiH_6) confirm the ductile nature of both hydrides. This ductility implies that Li_2SiH_6 and Na_2SiH_6 can withstand mechanical deformation without brittle fracture during repeated hydrogen absorption and desorption cycles [77]. Consequently, their resistance to pulverization is enhanced, which is critical for maintaining structural integrity, reversible capacity, and long-term cycling stability in practical hydrogen storage applications. This adaptability facilitates numerous loading and unloading cycles,

Table 3
Elastic constants (C_{ij}) and calculated Cauchy pressure (C_P) for A_2SiH_6 (A = Li and Na) hydrides.

Material	C_{11} (GPa)	C_{12} (GPa)	C_{44} (GPa)	$C_{11} + 2C_{12}$	$C_{11} - C_{12}$	C_P (GPa)
Li_2SiH_6	45.28	27.05	20.32	99.38	18.23	6.73
Na_2SiH_6	48.97	25.25	19.30	99.47	23.72	5.95

Table 4
The calculated values of Bulk modulus (B), Shear modulus (G), Young's modulus (E), B/G, and Poisson's ratio (ν) for A_2SiH_6 (A = Li and Na) perovskites.

Material	B (GPa)	G (GPa)	E (GPa)	B/G	G/B	ν
Li_2SiH_6	33.13	14.73	38.49	2.25	0.44	0.306
Na_2SiH_6	33.15	15.88	41.07	2.09	0.48	0.294

ensuring a robust and durable storage system essential for effective and efficient hydrogen utilization [78,79].

The anisotropy factor (A) is highly important in numerous applications, such as plastic deformation, phonon modes, and crack behavior [80,81]. *A* comprehensive analysis of this mechanical factor is essential to ascertain the extent of anisotropy in the atomic bonds across various plane orientations. When the value of A is 1 or deviates from 1, the system in question is characterized as either isotropic or anisotropic. The Zener anisotropy index A_Z, Chung-Buessem anisotropy index A_G, and universal elastic anisotropy index A_U for A_2SiH_6 hydrides are calculated from the following equations [82–84].

$$A_U = 5\frac{G_V}{G_R} + \frac{B_V}{B_R} - 6 \tag{14}$$

$$A_Z = \frac{2C_{44}}{(C_{11} - C_{12})} \tag{15}$$

$$A_G = \frac{(G_V - G_R)}{(G_V + G_R)} \times 100\% \tag{16}$$

G_V and B_V represent the shear and bulk moduli derived from the Voigt approximation. Furthermore, the shear and bulk moduli derived from the Reuss approach are represented by G_R and B_R, respectively. The crystal exhibits isotropy when the universal isotropic index (A_U) is equal to zero. The divergence of this value from zero signifies the extent of elastic anisotropy. The isotropy value for A_Z is 1, while A_G and A_U both register at zero. The degree of elastic anisotropy in a crystal is determined by values that fall below or exceed certain thresholds. $A_G = 1$ establishes the upper limit of elastic anisotropy. As shown in Table 5, Li_2SiH_6 and Na_2SiH_6 hydrides exhibit anisotropic characteristics.

The VELAS code [43] was employed to illustrate the influence of anisotropy on mechanical properties in three dimensions. The variation from sphericity in the figures generated using the VELAS code reflects the extent of anisotropy in the three-dimensional mechanical characteristics. Fig. 3 and Table 6 illustrate that A_2SiH_6 materials exhibit anisotropy in all mechanical properties, including Young's modulus E (GPa), Shear modulus G (GPa), and Poisson's ratio (ν), except for linear compression (β (TPa^{-1})).

The 3D anisotropy plots presented in Fig. 3 demonstrate the directional dependence of mechanical properties for Li_2SiH_6 and Na_2SiH_6. Quantitatively, as summarized in Tables 5 and 6, Li_2SiH_6 shows higher shear modulus anisotropy ($G^{max}/G^{min} = 2.23$) compared to Na_2SiH_6 (1.68). Similarly, Young's modulus anisotropy ratios indicate Li_2SiH_6 ($E^{max}/E^{min} = 2.02$) is more anisotropic than Na_2SiH_6 (1.57). The higher A_G, A_Z, and A_U indices in Li_2SiH_6 further confirm its greater elastic anisotropy.

From an application perspective, elastic anisotropy can influence mechanical processing, shaping, and integration into solid-state hydrogen storage systems or composite structures. Higher anisotropy may lead to direction-dependent deformation or stress accumulation, which can cause microcrack initiation under cyclic hydrogen absorption-desorption [85]. In contrast, lower anisotropy, as observed in Na_2SiH_6, suggests more uniform mechanical responses, which is beneficial for structural stability and device reliability.

In addition, various mechanical parameters such as density (ρ), longitudinal wave velocity (v_l), transverse wave velocity (v_t), average wave velocity (v_m), Debye temperature (Θ_D), and melting temperature (T_M) of A_2SiH_6 have been computed, as shown in Table 7 [81]. The Debye temperature, which provides an estimation of the thermal stability and phonon-related features, is greater for Li_2SiH_6 (605.01 K) than for Na_2SiH_6 (502.45 K), suggesting sturdier atomic bonding in the Li-containing material.

Moreover, the melting temperature (T_M) is a critical parameter that influences the application of crystal in heating systems, with the melting temperature values of these compounds presented in Table 7.

In summary, elastic properties and the mechanical stability of A_2SiH_6 double perovskite hydrides indicate that both materials are mechanically ductile and robust. Li_2SiH_6 demonstrates marginally greater thermal stability and stiffness, yet Na_2SiH_6 shows inferior shear anisotropy, which may make it more susceptible to structural distortions. These results contribute to the emphasis on A_2SiH_6 compounds as potential candidates for hydrogen storage applications.

Table 5
Elastic anisotropy parameters for A_2SiH_6 (A = Li and Na) perovskites.

Material	G_V (GPa)	B_V (GPa)	G_R (GPa)	B_R (GPa)	A_U	A_Z	A_G
Li_2SiH_6	15.84	33.13	13.62	33.13	0.81	2.23	7.52
Na_2SiH_6	16.32	33.15	15.43	33.15	0.29	1.68	2.82

3.3. Electronic band structure and density of states analysis

Understanding the electronic characteristics of A_2SiH_6 (A = Li and Na) double perovskite hydrides has been crucial for evaluating their potential in optoelectronic and hydrogen storage applications [86]. We used both GGA-PBE and HSE06 functionals to find the electronic band structures and partial and total densities of states (PDOS/TDOS) for these compounds. As seen in Figs. 4(a) and 5(a), using GGA-PBE to do electronic band structure computations showed that Li_2SiH_6 and Na_2SiH_6 exhibit indirect band gaps of 1.28 eV and 1.44 eV, respectively. However, it is well established that standard GGA functionals tend to underestimate the band gap values due to their approximate treatment of exchange-correlation effects. To obtain more accurate predictions, additional calculations were performed using the HSE06 functional. The HSE06 results showed that Li_2SiH_6 has an increased indirect band gap of 2.22 eV, while Na_2SiH_6 has an indirect band gap of 2.32 eV, as seen in Figs. 4(b) and 5(b). These band gaps are much larger than those obtained from GGA-PBE calculations, demonstrating that hybrid functional methods are necessary for accurate electronic property assessments. While GGA-PBE provides a qualitative understanding of the semiconducting behavior, HSE06 offers quantitatively improved estimates that are critical for optoelectronic and energy-related application evaluations. Furthermore, the determined band gap values indicate that Na_2SiH_6 exhibits a slightly wider band gap compared to Li_2SiH_6, which may influence their optical absorption characteristics. This difference primarily arises from the variation in the atomic radii of Li and Na, affecting the hybridization and dispersion of electronic bands.

In comparison with other reported A_2BH_6-type hydrides, HSE06-calculated band gaps of Li_2SiH_6 (2.22 eV) and Na_2SiH_6 (2.32 eV) are significantly higher than those of K_2GeH_6 (1.897 eV) and Rb_2GeH_6 (2.129 eV) and are slightly lower than K_2SnH_6 (2.468 eV) and Rb_2SnH_6 (2.657 eV) [86]. This trend reflects the influence of A-site cation size, where the substitution of larger cations such as Na or Rb leads to wider band gaps, similar to how Rb-based hydrides exhibit larger band gaps than their K-based analogs. Overall, the systematically larger band gaps obtained using HSE06 for these perovskite hydrides emphasize the importance of employing hybrid functionals for accurate prediction of their electronic and optoelectronic properties, thereby guiding their potential application in UV optoelectronic devices and hydrogen storage systems.

The HSE06 results showed that Li_2SiH_6 has an increased indirect band gap of 2.22 eV, while Na_2SiH_6 has an indirect band gap of 2.32 eV, as seen in Figs. 4(b) and 5(b). These band gaps from HSE06 are much bigger than the ones from GGA-PBE, which shows that hybrid functional methods are needed for accurate electronic property assessment. This comparison highlights that while GGA-PBE provides a qualitative understanding of the semiconducting behavior, HSE06 offers quantitatively improved estimates critical for optoelectronic and energy-related application assessments. Furthermore, the determined bandgap values suggest that Na_2SiH_6 exhibits a wider bandgap compared to Li_2SiH_6, potentially influencing their optical absorption characteristics. The

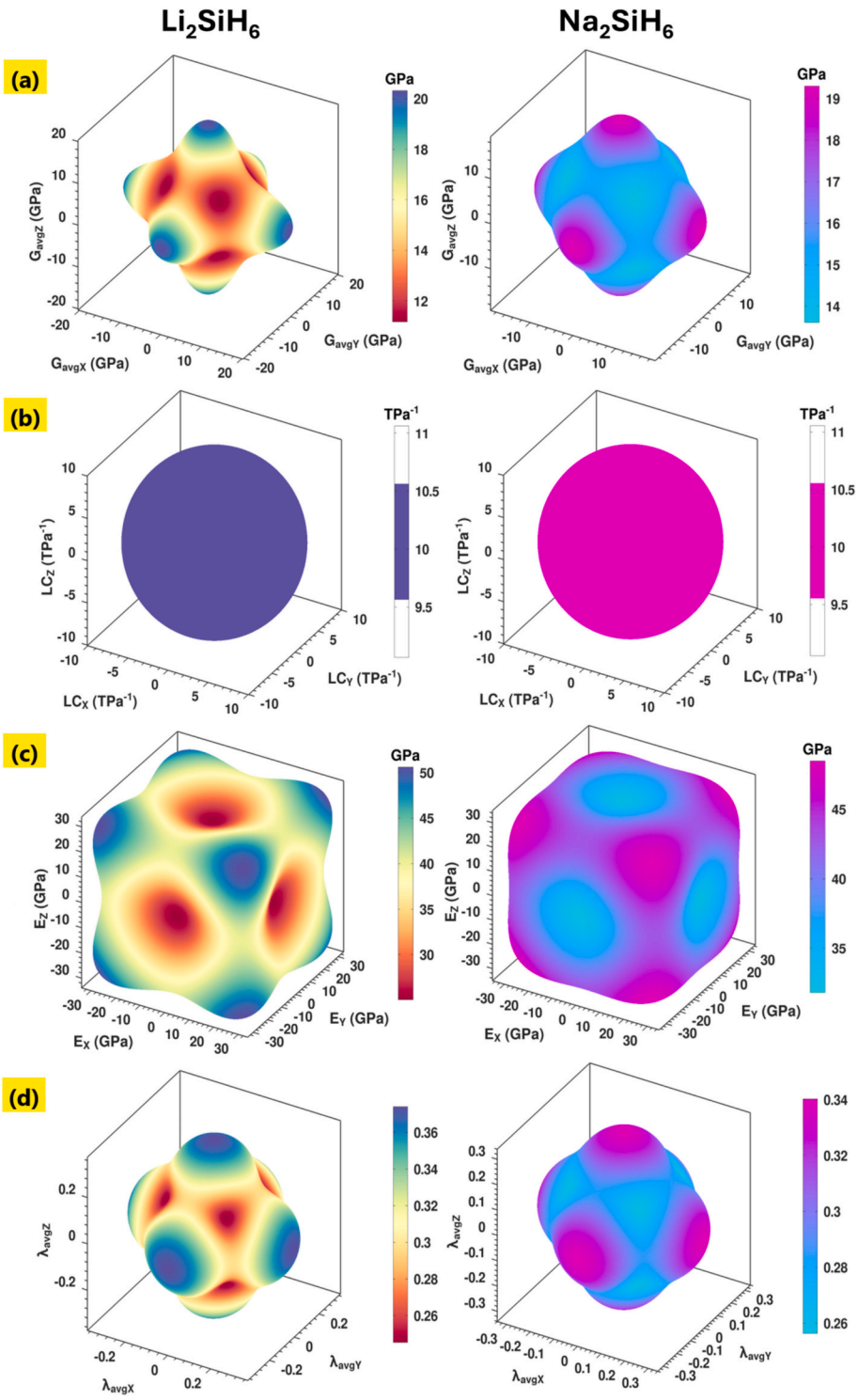

Fig. 3. The elastic anisotropy modules in 3D (a) Shear modulus (G), (b) linear compression (β), (c) Young modulus (E), (d) Poisson's ratio (υ) of Li_2SiH_6 and Na_2SiH_6.

observed differences primarily arise from the variation in atomic radii of Li and Na, which influences the hybridization of electronic bands and their dispersion characteristics.

To better understand the electronic structure of A_2SiH_6 (A = Li and Na) double perovskite hydrides, the total and partial density of states (TDOS and PDOS) were calculated using the GGA-PBE and HSE06 methods, as shown in Figs. 4 and 5. The PDOS results indicate that in both Li_2SiH_6 and Na_2SiH_6, the valence band is predominantly composed of H-*s* and Si-*p* orbitals, reflecting strong hybridization between hydrogen and silicon. The conduction band mainly arises from Si-*p* and A-2 *s*/3 *s* (A = Li, Na) states. The robust hybridization among H and Si orbitals indicates covalent bonding features, which play a decisive role in the stability of these perovskite hydrides.

The electronic density distribution and the indirect bandgap nature suggest that A_2SiH_6 (A = Li and Na) hydrides acquire moderate electronic conductivity, which may influence their performance in optoelectronic applications and solid-state hydrogen storage. The next section further explores their optical features to evaluate their suitability for such functions.

Table 6
The calculated minimum and maximum values of Shear modulus (G), linear compression (β), Young's modulus (E), and Poisson's ratio (ν) of A_2SiH_6 (A = Li and Na) perovskite hydrides.

Material	G (GPa)		β (TPa^{-1})		E (GPa)		ν	
	G_{min}	G_{max}	β_{min}	β_{max}	E_{min}	E_{max}	ν_{min}	ν_{max}
Li_2SiH_6	9.12	20.32	10.06	10.06	25.05	50.61	0.00	0.60
Anisotropy	2.23		1.00		2.02		∞	
Na_2SiH_6	11.86	19.3	10.05	10.05	31.79	48.49	0.11	0.46
Anisotropy	1.68		1.00		1.57		4.16	

Table 7
The calculated density (ρ), longitudinal wave velocity (v_l), transverse wave velocity (v_t), average wave velocity (v_m), Debye temperature (Θ_D), and melting temperature (T_M) of A_2SiH_6 (A = Li and Na).

Material	ρ (g/cm^3)	v_l (m/s)	v_t (m/s)	v_m (m/s)	Θ_D(K)	T_M
Li_2SiH_6	1.129	6837	3612	4038	605.01	821
Na_2SiH_6	1.533	5953	3218	3592	502.45	842

3.4. Optical properties

Examining the optical features of crystals delivers valuable insights into their interaction with electromagnetic waves. This information is important for determining electronic transitions, band gaps, and overall optical behavior [87]. It is also necessary for measuring the performance of compounds. Optical analysis is also a key part of understanding how hydrogen desorbs and absorbs are important for solid-state hydrogen storage. The optical features of A_2SiH_6 (A = Li and Na) double perovskite hydrides have been examined to evaluate their potential for optoelectronic applications. The real and imaginary components of the dielectric function ε (ω), optical conductivity σ (ω), refractive index n (ω), absorption coefficient I (ω), and reflectivity R (ω) have been computed and shown in Fig. 6(a–f) [88].

The dielectric function ε (ω) is essential for comprehending the optical and electrical characteristics of materials, including their responses to light, electromagnetic waves, and electronic conduction. The complex ε (ω) comprises two components and the optical dielectric function expression is [87]:

$$\varepsilon(\omega) = \varepsilon_1(\omega) + i\varepsilon_2(\omega) \tag{17}$$

The real part $\varepsilon_1(\omega)$ demonstrates the dispersion and polarization of materials, and the imaginary part $\varepsilon_2(\omega)$ indicates the absorption characteristics. The real $\varepsilon_1(\omega)$ and imaginary parts $\varepsilon_2(\omega)$ of the optical dielectric function for A_2SiH_6 (A = Li and Na) double perovskite hydrides were determined, as shown in Fig. 6(a) and (b).

Fig. 6(a) shows that the static dielectric constant ε_1 (0) is 4.35 for Li_2SiH_6 and 3.37 for Na_2SiH_6, as indicated by the initial values of their respective curves. As photon energy rises, the real part of the dielectric

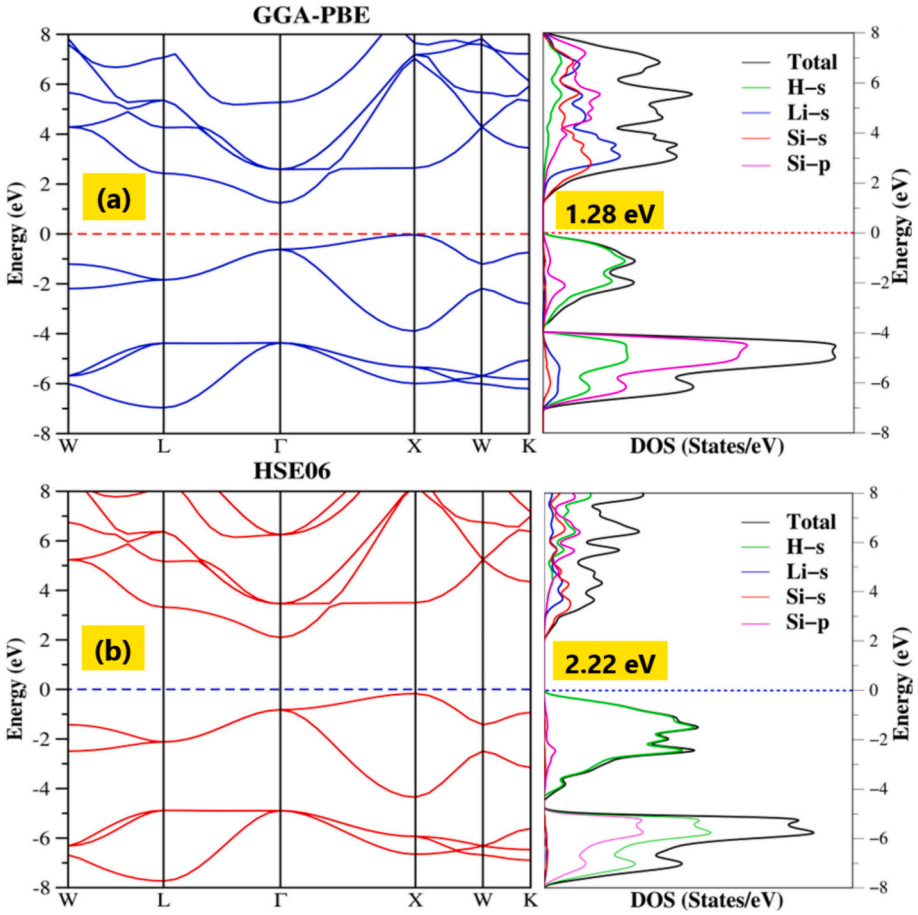

Fig. 4. The electronic band structure and total and partial density of states (TDOS/PDOS) of Li_2SiH_6 using (a) GGA-PBE and (b) HSE06 functionals.

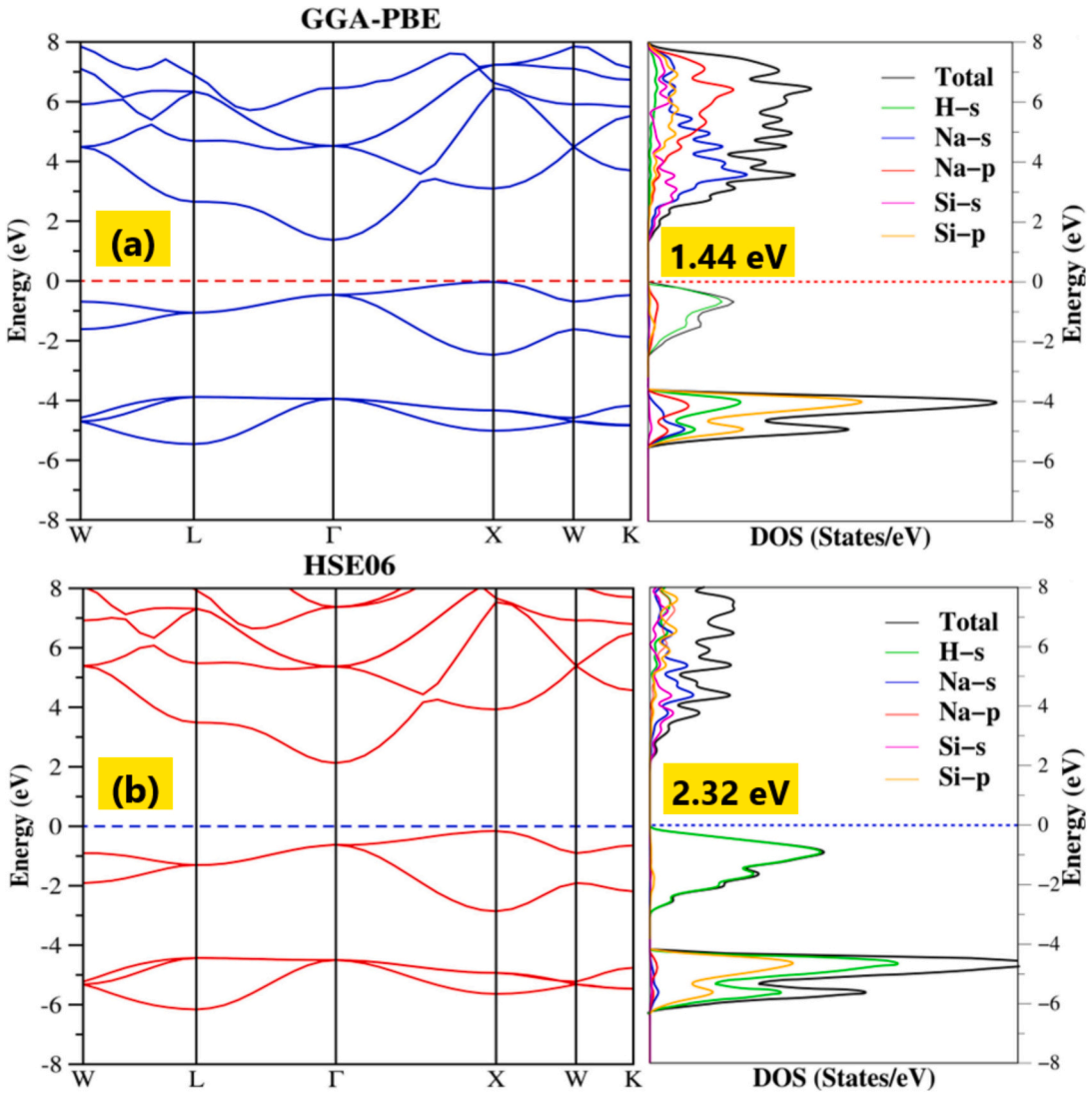

Fig. 5. The electronic band structure and total and partial density of states (TDOS/PDOS) of Na_2SiH_6 using (a) GGA-PBE and (b) HSE06 functionals.

function for these hydrides reaches a maximum of 8.19 eV and 6.51 eV, respectively. Subsequently, it dropped to negative values with −2.19 at 9.45 eV and −1.19 at 10.13 eV for Li_2SiH_6 and Na_2SiH_6. The results indicate that the real part of the dielectric function for these two compounds follows a parallel trend.

Fig. 6(b) illustrates the imaginary part of the dielectric function $\varepsilon_2(\omega)$ for Li_2SiH_6 and Na_2SiH_6, respectively. In the photon energy range of 0–2.3 eV, the imaginary part curves of these compounds approach zero, signifying minimal light absorption. The determined optical bandgap values from $\varepsilon_2(\omega)$ are 2.21 eV for Li_2SiH_6 and 2.33 eV for Na_2SiH_6, which align well with the anticipated bandgap based on electronic characteristics. As photon energy escalates from 2 to 8 eV, these compounds attain their optimal light absorption, with peak $\varepsilon_2(\omega)$ values occurring at around 6.67 (6.99) eV. Namely, the maximum peak values in the spectra of $\varepsilon_2(\omega)$ are found in the ultraviolet portions of the electromagnetic spectrum. A decline towards zero is evident in the spectra of these compounds when photon energy increases from 8 to 24 eV. The examined compounds are significant candidates for optoelectronic devices. As a result, the findings showed that Li_2SiH_6 has a better dielectric function than Na_2SiH_6, which is affected by electronic polarizability and charge carrier density. Materials with elevated dielectric function are essential in several applications, including capacitors, photonics, optoelectronics, and energy storage [89,90].

Optical conductivity σ (ω) is a crucial physical parameter that quantifies a material's efficiency in converting absorbed light energy into electrical energy [87]. Materials with high optical conductivity are more efficient at absorbing light energy and converting it into electrical energy, while those with poor optical conductivity are less efficient in this conversion process. Fig. 6(c) shows the optical conductivity for A_2SiH_6 (A = Li and Na) double perovskite hydrides. Observations show that these compounds have optical conductivity approaching zero. This is in agreement with their semiconductor properties. This result indicates that there is no photon absorption below the band gaps. The maximum σ (ω) values for these hydrides occur at 6.83 eV for Li_2SiH_6 and 7.54 eV for Na_2SiH_6, placing them within the ultraviolet region of the electromagnetic spectrum.

The refractive index n (ω) is a fundamental physical parameter that characterizes a material's capacity to refract incoming light radiation [87]. It is connected to the optical characteristics of the material and directly influences the propagation of light inside it. Fig. 6(d) displays the refractive index curves n (ω) of A_2SiH_6 (A = Li and Na). In the photon energy range of 0–6 eV, the refractive index curves of these compounds exhibit a rise, reaching a maximum of around 6 eV. In the 6–14 eV range, the refractive index of A_2SiH_6 (A = Li and Na) compounds diminishes as photon energy increases, approaching zero. On the other hand, the refractive index value at zero frequency (ω = 0) is specified as a static

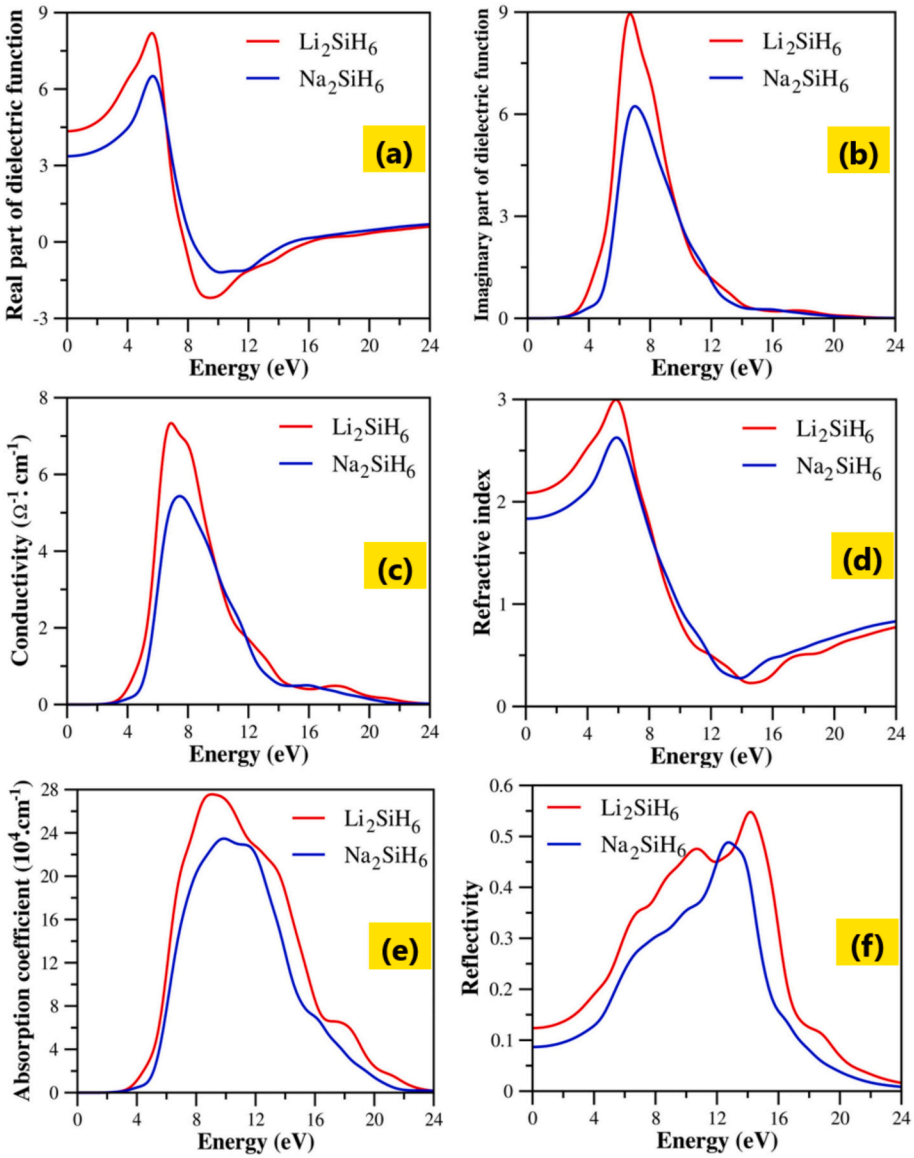

Fig. 6. The real (a) and imaginary (b) parts of the dielectric function, (c) Optical conductivity, (d) Refractive index, (e) Absorption coefficient, and (f) Reflectivity for A_2SiH_6 (A = Li and Na).

constant, denoted as n (0), for these semiconductor compounds. The static refractive indices of these substances are 2.09 and 1.83, respectively. This finding indicates a high link between the static refractive index n (0) and ε_1 (0), as shown by the following relationship [66]:

$$n\,(0) = \sqrt{\varepsilon_1\,(0)} \tag{18}$$

The optical absorption coefficient I (ω) [87] is a crucial parameter for characterizing a material's capacity to absorb light. An elevated absorption coefficient signifies the substance's enhanced ability to absorb light. Fig. 6(e) illustrates the optical absorption coefficient curves I (ω) of the A_2SiH_6 (A = Li and Na) hydrides. In the 0–2.5 eV energy spectrum, the optical absorption coefficients of the A_2SiH_6 (A = Li and Na) compounds are near zero, signifying their limited capacity to absorb light in this range. Li_2SiH_6 and Na_2SiH_6 exhibit strong absorption peaks around ~7 eV, corresponding to the deep UV (DUV) spectral region (≈177 nm). They are especially appropriate for applications in DUV photodetectors (flame detection, sterilization monitoring, UV astronomy), DUV-transparent optical materials, and gas sensors. These hydride-based structures provide strong spectrum selectivity due to their steep absorption curves, along with notable benefits like minimal toxicity and simplicity of production. In the 7–12 eV energy range, the optical absorption coefficient curves for these compounds exhibit similarities, indicating superior photon absorption efficiency in this range.

Finally, Fig. 6(f) displays the reflectivity spectra R (ω), providing evidence of surface interactions with light [87]. From Fig. 6(f), the static reflectivity values R (0) for Li_2SiH_6 and Na_2SiH_6 are 0.124 and 0.087, respectively. Across the 10–14 eV range of photon energy, reflectivity peaks occur for these compounds. The low reflectivity in the visible area designates minimal optical losses, which is an advantageous characteristic for transparent conducting compounds and photovoltaic devices.

In summary, the optical breakdown of A_2SiH_6 perovskite hydrides discloses that these compounds have potential optoelectronic applications, predominantly in UV-responsive devices. Their robust dielectric response, high refractive index, and efficient absorption in the UV range brand them as promising candidates for optical coatings, sensors, and energy-harvesting technologies.

3.5. Dynamic stability

To investigate the dynamic stability of double perovskite hydrides

A_2SiH_6 (A = Li and Na), phonon dispersion calculations along the high-symmetry directions of the Brillouin zone were performed and presented in Fig. 7(a) and (b). The obtained phonon spectra for both Li_2SiH_6 and Na_2SiH_6 reveals the presence of imaginary (negative) frequencies, predominantly in the low-frequency acoustic branches. This behavior, as shown in Fig. 7(a) and (b), indicates dynamic lattice instability and suggests a tendency for structural distortions or possible phase transitions under ambient conditions. Such results imply that while these hydrides may be thermodynamically stable, they could require external stabilization, such as high pressure or temperature effects, to maintain their cubic perovskite structure.

Such imaginary phonon modes are not uncommon in hydride compounds with high hydrogen concentration. Similar dynamic instabilities under ambient conditions have been reported for other perovskite hydrides, such as K_2NaXH_6 (X = As, Bi, In) [91], $AlFe_3H$, $GaFe_3H$, and $InFe_3H$ [92], as well as for $AlCa_3H_9$ and $AlSc_3H_9$ materials [93]. Additionally, recent studies on double perovskites such as K_2TlZl_6 (Z = Al, In) have also shown the occurrence of imaginary phonon frequencies, which are attributed to soft phonon modes associated with possible structural phase transitions [94]. In these crystals, the presence of negative phonon branches is not necessarily interpreted as a serious defect in structural integrity; rather, it is often considered an indication of possible soft lattice modes that may facilitate hydrogen release. This characteristic could be beneficial for enhancing hydrogen desorption kinetics. Moreover, previous studies have suggested that such dynamic instabilities can be alleviated through the application of external pressure or by considering finite temperature effects. For instance, applying a moderate hydrostatic pressure (approximately 6 GPa) has been shown to stabilize $AlSc_3H_9$ [93], while molecular dynamics simulations performed at room temperature confirmed its thermodynamic viability despite its instability at 0 K [95]. Therefore, it is plausible to expect that the A_2SiH_6 (A = Li and Na) double perovskite hydrides examined in this study may also exhibit stabilized phonon behavior under applied pressure or elevated temperature conditions. This highlights the importance of conducting further finite-temperature ab initio molecular dynamics (AIMD) simulations to comprehensively evaluate their potential structural stability and practical applicability.

3.6. Molecular dynamics simulation

The thermal and vibrational behaviors of A_2SiH_6 (A = Li and Na) double perovskite hydrides were investigated using ab initio molecular dynamics (AIMD) simulations under NVT ensembles at 300 K for 5000 fs to complement the phonon dispersion results [96,97]. Phonon calculations revealed the presence of imaginary (negative) frequencies, predominantly in the low-frequency acoustic branches, suggesting dynamic lattice instability and a potential tendency for structural distortions or phase transitions at 0 K. However, AIMD simulations provide further insight into their practical stability under finite temperature conditions. As shown in Fig. 8(a–d), both Li_2SiH_6 and Na_2SiH_6 exhibit only minor fluctuations in total energy while maintaining constant temperature profiles throughout the simulation duration. These results indicate that despite the predicted dynamic instabilities from phonon calculations at absolute zero, both hydride structures preserve their structural integrity and remain thermally stable at room temperature. Therefore, Li_2SiH_6 and Na_2SiH_6 emerge as promising candidates for hydrogen storage and other energy-related applications due to their dynamic and thermal stability under operational conditions. Particularly in energy storage systems where thermal endurance is critical, our findings provide a solid foundation supporting the practical applicability of these materials.

4. Conclusion

This study comprehensively investigates the structural, mechanical, electronic, thermal, dynamic, and optical properties of A_2SiH_6 (A = Li and Na) double perovskite hydrides using first-principles calculations based on density functional theory (DFT). The calculated tolerance factors suggest that both Li_2SiH_6 and Na_2SiH_6 adopt stable cubic perovskite structures. Their thermodynamic stability is confirmed by negative formation energies, with Na_2SiH_6 exhibiting slightly greater stability than Li_2SiH_6. The gravimetric hydrogen storage capacities are calculated to be 12.60 wt% for Li_2SiH_6 and 7.55 wt% for Na_2SiH_6, highlighting their significant potential for hydrogen storage applications. However, the desorption temperatures of Li_2SiH_6 (107.78 K) and Na_2SiH_6 (123.88 K) are below the recommended range (233−333 *K*) specified by the US Department of Energy for practical hydrogen storage systems, suggesting that further material modification or doping strategies may be required to optimize their desorption behavior.

The elastic constants of both hydrides satisfy the Born stability criteria, confirming their mechanical stability, while the estimated bulk and shear moduli indicate that Li_2SiH_6 is slightly stiffer than Na_2SiH_6. Moreover, positive Cauchy pressures and B/G ratios greater than 1.75 reveal their ductile nature, suggesting suitability for efficient hydrogen storage without structural failure during cyclic loading. Electronic band

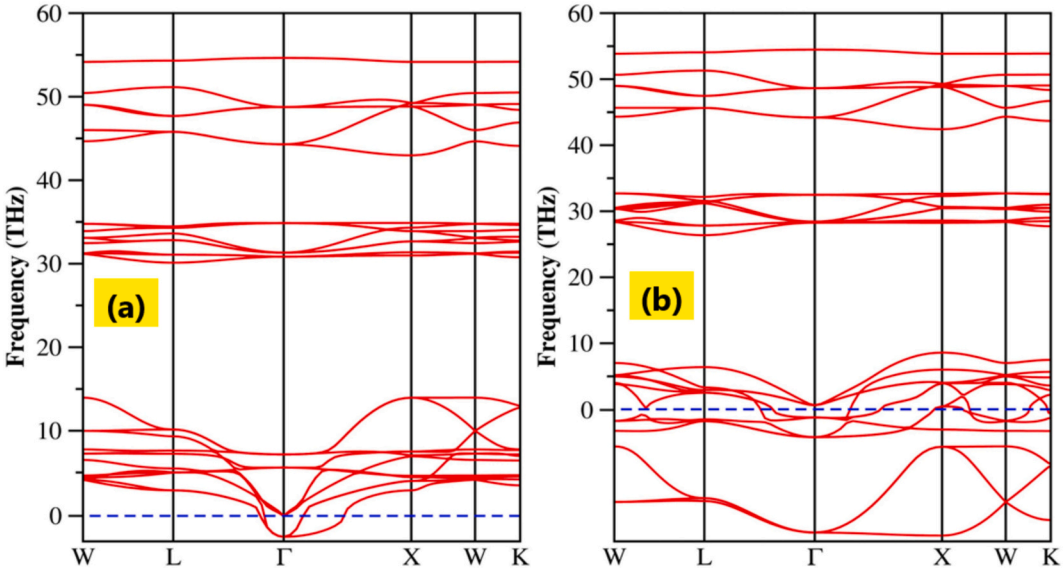

Fig. 7. The phonon dispersion curve of the double perovskite hydride (a) Li_2SiH_6 and (b) Na_2SiH_6.

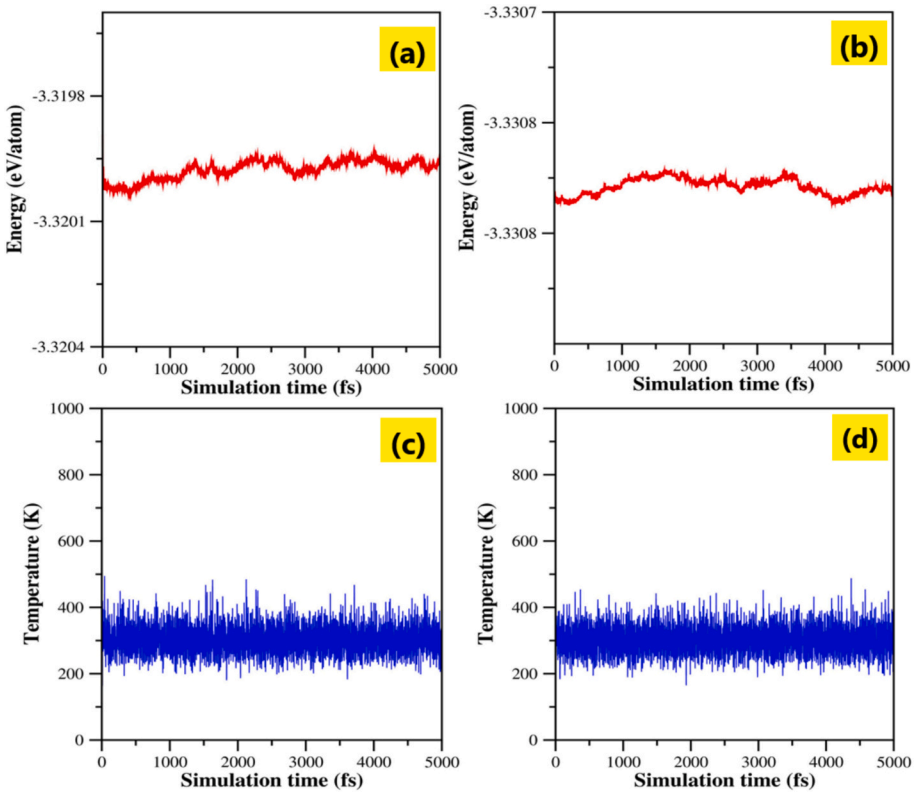

Fig. 8. The AIMD simulation of energy and temperature as a function of time for (a, c) Li_2SiH_6 and (b, d) Na_2SiH_6.

structure calculations indicate semiconducting behavior with indirect band gaps of 1.28 eV for Li_2SiH_6 and 1.44 eV for Na_2SiH_6 at the GGA-PBE level, while hybrid functional (HSE06) results show increased indirect band gaps of 2.22 eV and 2.32 eV, respectively. Density of states analysis reveals significant hybridization between Si and H orbitals, contributing to the compounds' structural stability and electronic characteristics. Furthermore, the optical properties, including dielectric function, refractive index, and absorption coefficient, are evaluated to provide a comprehensive understanding of their electronic and optical behavior. Overall, these findings demonstrate that A_2SiH_6 (A = Li and Na) double perovskite hydrides exhibit favorable structural, electronic, thermodynamic, thermal, and mechanical properties, supporting their potential as promising candidates for solid-state hydrogen storage applications.

CRediT authorship contribution statement

Abdullah Candan: Writing – original draft, Visualization, Methodology, Formal analysis, Data curation, Investigation, Software, Supervision, Writing – review & editing. **Aytac Erkisi:** Writing – review & editing, Writing – original draft, Methodology, Conceptualization, Investigation. **Bugra Yildiz:** Writing – original draft, Visualization, Investigation, Data curation, Formal analysis, Software, Writing – review & editing.

Declaration of competing interest

The authors declare that they have no known competing financial interests or personal relationships that could have appeared to influence the work reported in this paper.

Acknowledgments

This research was supported in part by TÜBİTAK (The Scientific & Technological Research Council of Turkey) through TR-Grid e-Infrastructure Project, part of the calculations has been carried out at ULAKBİM Computer Center.

Data availability

Data will be made available on request.

References

[1] R. Murphy, What is undermining climate change mitigation? How fossil-fuelled practices challenge low-carbon transitions, Energy Res. Soc. Sci. 108 (2024) 103390.
[2] Y.L. Zhang, A.Z. Han, S.Z. Deng, X.W. Wang, H.H. Zhang, S. Hajat, J.S. Ji, W. N. Liang, C.R. Huang, The impact of fossil fuel combustion on children's health and the associated losses of human capital, Global Transit. 5 (2023) 117–124.
[3] A.K. Arshad, N. Hussain, M.H. Ashraf, M.Z. Saleem, Air pollution and climate change as grand challenges to sustainability, Sci. Total Environ. 928 (2024) 172370.
[4] O. Sadeghian, B. Mohammadi-Ivatloo, A. Oshnoei, J. Aghaei, Unveiling the potential of renewable energy and battery utilization in real-world public lighting systems: a review, Renew. Sustain. Energy Rev. 192 (2024) 114241.
[5] J. Jurasz, F.A. Canales, A. Kies, M. Guezgouz, A. Beluco, A review on the complementarity of renewable energy sources: concept, metrics, application and future research directions, Sol. Energy 195 (2020) 703–724.
[6] M.K. Shahzad, S.T. Mujtaba, S. Hussain, J.U. Rehman, M.U. Farooq, M.A. Khan, M. B. Tahir, M.A. Mahmood, Zirconium-based cubic-perovskite materials for photocatalytic solar cell applications: a DFT study, RSC Adv. 12 (42) (2022) 27517–27524.
[7] X.Y. Wang, H.R. Liu, K. Khalid, Innovation in technology: a game changer for renewable energy in the European Union? Nat. Res. Forum (2024) 03–16.
[8] J. Li, T.G. Lu, X.N. Yi, R. Hao, Q. Ai, Y. Guo, M.L. An, S.R. Wang, X.Q. He, Y.X. Li, Concentrated solar power for a reliable expansion of energy systems with high renewable penetration considering seasonal balance, Renew. Energy 226 (2024) 120089.
[9] A.S. Mekonnin, K. Wacławiak, M. Humayun, S. Zhang, H. Ullah, Hydrogen storage technology, and its challenges: a review, Catalysts 15 (2025) 260.
[10] O. Faye, J. Szpunar, U. Eduok, A critical review on the current technologies for the generation, storage, and transportation of hydrogen, Int. J. Hydrogen Energy 47 (2022) 13771–13802.

[11] A.M. Abdalla, S. Hossain, O.B. Nisfindy, A.T. Azad, M. Dawood, A.K. Azad, Hydrogen production, storage, transportation and key challenges with applications: a review, Energ. Conver. Manage. 165 (2018) 602–627.

[12] S. Bosu, N. Rajamohan, Recent advancements in hydrogen storage – comparative review on methods, operating conditions and challenges, Int. J. Hydrogen Energy 52 (2024) 352–370.

[13] D. Tang, G.L. Tan, G.W. Li, J.G. Liang, S.M. Ahmad, A. Bahadur, M. Bououdina, State-of-the-art hydrogen generation techniques and storage methods: a critical review, J. Energy Storage 64 (2023) 107196.

[14] S. Ahmad, A. Ullah, A. Samreen, M. Qasim, K. Nawaz, W. Ahmad, M. Egilmez, Hydrogen production, storage, transportation and utilization for energy sector: a current status review, J. Energy Storage 101 (2024) 113733.

[15] N. Klopčič, I. Grimmer, F. Winkler, M. Sartory, A. Trattner, A review on metal hydride materials for hydrogen storage, J. Energy Storage 72 (2023) 108456.

[16] Y. Wang, J.X. Ma, J. Ren, D. Zhang, F.Y. Xu, K. Zhang, H.H. Chen, Hydrogen production from hydrolysis of $NaBH_4$ solution over Co–Fe–B@g–C_3N_4/NF thin film catalyst, Rare Metals 43 (2024) 2648–2659.

[17] Z.Y. Li, L.X. Sun, F. Xu, Y.M. Luo, Y.P. Xia, S. Wei, H.G. Pan, Modulated noble metal/2D MOF heterostructures for improved hydrogen storage of MgH_2, Rare Metals 43 (2024) 1672–1685.

[18] Y. Liu, P.P. Zhou, X.Z. Xiao, J.C. Qi, J.P. Bi, T. Ying, L.X. Chen, Deep insight of unique phase transition behaviors and mechanism in Zr_2Co–H isotope system with ultra-low equilibrium pressure, Rare Metals 43 (2024) 212–224.

[19] Z.Y. Liu, S. Yang, Y.Y. Yang, W.Y. Guo, J.F. Wang, B.X. Wang, X. Gao, T. Wang, S. J. Liu, Z.L. Yu, Efficient hydrogen production from high-concentration aqueous formic acid over bio-based γ-Mo_2N catalysts, Carbon Resour. Convers. 7 (2024) 100209.

[20] Y.B. Shen, Z.L. Yang, X.M. Tang, J.M. Zhang, G.J. Lv, Hydrogen production through distinctive C-C cleavage during acetic acid reforming at low temperature, ChemSusChem 17 (2024) e202301532.

[21] J.R. Rostrup-Nielsen, Conversion of hydrocarbons and alcohols for fuel cells, Phys. Chem. Chem. Phys. 3 (2001) 283–288.

[22] M. Caid, D. Rached, Y. Rached, H. Rached, Exploring the versatile properties of $Cs_2B'GeF_6$ (B′: Sn, Pb) double perovskites: Insights into their mechanical stability, optoelectronic potential, and high thermoelectric performance, Phys. B Condens. Matter 677 (2024) 415742.

[23] M. Caid, Y. Rached, D. Rached, H. Rached, First principles study of the structural, elastic, magneto-electronic and thermoelectric properties of double perovskite Ba_2ZrFeO_6 in ferrimagnetic phase, Comput. Condens. Matter 37 (2023) e00847.

[24] H. Rached, D. Rached, M. Caid, L. Amrani, Y. Rached, H. Mansour, A.A. Belkacem, Future insights into double perovskites Ba_2AlTMO_6 (TM = W, Re, Os) for sustainable and clean energy production: a DFT investigation using GGA, TB-mBJ, and HSE06 methods, J. Inorg. Organomet. Polym. Mater. 1–22 (2025).

[25] M. Caid, H. Rached, D. Rached, Y. Rached, Investigation of structural, elastic, electronic, and optical properties of lead-free double perovskites Cs_2XBeBr_6 (X = Ge, Sn): a first-principles DFT study, J. Mol. Model. 30 (2024) 354.

[26] M. Caid, D. Rached, Y. Rached, H. Rached, Comprehensive exploration of halide double perovskites $Cs_2B'GeCl_6$ (B′: Zn, Cd) for affordable energy technologies: a high-throughput investigation, Opt. Quant. Electron. 56 (2024) 980.

[27] M. Caid, D. Rached, H. Rached, Y. Rached, A density functional theory exploration of $Cs_2B'B''I_6$ (B′B″: BeCa, BeSr, GeCd, GeBe, GeMg) halide double perovskites for optimal solar cell and renewable energy applications, Phys. Status Solidi B 261 (2024) 2300577.

[28] T. Liang, Z. Zhang, X. Feng, H. Jia, C.J. Pickard, S.A.T. Redfern, et al., Ternary hypervalent silicon hydrides via lithium at high pressure, Phys. Rev. Mater. 4 (2020) 113607.

[29] T. Liang, Z. Zhang, H. Yu, T. Cui, X. Feng, C.J. Pickard, et al., Pressure-induced superionicity of H^- in hypervalent sodium silicon hydrides, J. Phys. Chem. Lett. 12 (2021) 7166–7172.

[30] P. Zhang, Y. Sun, X. Li, J. Lv, H. Liu, Structure and superconductivity in compressed Li-Si-H compounds: density functional theory calculations, Phys. Rev. B 102 (2020) 184103.

[31] H. Xie, T. Liang, T. Cui, X. Feng, H. Song, D. Li, et al., Structural diversity and hydrogen storage properties in the system K–Si–H, Phys. Chem. Chem. Phys. 24 (2022) 13033–13039.

[32] S. Wu, B. Li, Z. Chen, Y. Hou, Y. Bai, X. Hao, et al., Phase transitions and superconductivity in ternary hydride Li_2SiH_6 at high pressures, J. Appl. Phys. 131 (2022) 065901.

[33] K. Puhakainen, D. Benson, J. Nylén, S. Konar, E. Stoyanov, K. Leinenweber, et al., Hypervalent octahedral SiH_6^{2-} species from high-pressure synthesis, Angew. Chem. Int. Ed. 51 (2012) 3156–3160.

[34] O.Y. Vekilova, D.C. Beyer, S. Bhat, R. Farla, V. Baran, S.I. Simak, et al., Formation and polymorphism of semiconducting K_2SiH_6 and strategy for metallization, Inorg. Chem. 62 (2023) 8093–8100.

[35] G. Kresse, J. Hafner, Ab initio molecular dynamics for liquid metals, Phys. Rev. B 47 (1993) 558–561.

[36] G. Kresse, J. Furthmuller, Efficiency of ab initio total energy calculations for metals and semiconductors using a plane-wave basis set, Comput. Mater. Sci. 6 (1996) 15–50.

[37] W. Kohn, L.J. Sham, Self-consistent equations including exchange and correlation effects, Phys. Rev. 140 (1965) A1133–A1138.

[38] P.E. Blöchl, Projector augmented-wave method, Phys. Rev. B 50 (1994) 17953–17979.

[39] H.J. Monkhorst, J.D. Pack, Special points for Brillouin-zone integrations, Phys. Rev. B 13 (1976) 5188.

[40] J.P. Perdew, K. Burke, M. Ernzerhof, Generalized gradient approximation made simple, Phys. Rev. Lett. 77 (1996) 3865–3868.

[41] J. Paier, M. Marsman, K. Hummer, G. Kresse, I.C. Gerber, J.G. Ángyán, Screened hybrid density functionals applied to solids, J. Chem. Phys. 124 (2006) 154709.

[42] K. Momma, F. Izumi, VESTA 3 for three-dimensional visualization of crystal, volumetric and morphology data, J. Appl. Cryst. 44 (6) (2011) 1272–1276.

[43] R. Zheng, C. Zou, Z. Wei, H. Wang, VELAS: An open-source toolbox for visualization and analysis of elastic anisotropy, Comput. Phys. Commun. 283 (2023) 108540.

[44] Y. Le Page, P. Saxe, Symmetry-general least-squares extraction of elastic data for strained materials from ab initio calculations of stress, Phys. Rev. B 65 (2002) 104104.

[45] K. Parlinski, Z.Q. Li, Y. Kawazoe, First-principles determination of the soft mode in cubic ZrO_2, Phys. Rev. Lett. 78 (1997) 4063.

[46] A. Togo, F. Oba, I. Tanaka, First-principles calculations of the ferroelastic transition between rutile-type and $CaCl_2$-type SiO_2 at high pressures, Phys. Rev. B 78 (2008) 134106.

[47] S. Al, Ç. Yamçıçıer, Computational exploration of hexahydride materials (K_2SiH_6 and Rb_2SiH_6); structural, mechanical, thermodynamic, optic, electronic and dynamic properties, J. Energy Storage 91 (2024) 112033.

[48] https://oqmd.org/materials/entry/1279113.

[49] M.A. Ghebouli, H. Choutri, N. Bouarissa, B. Ghebouli, A. Bouhemadou, F. Soyalp, H.Y. Ocak, Theoretical prediction of the fundamental properties for the ternary Li_2PtH_6 and Na_2PtH_6, J. Solid State Chem. 196 (2012) 498–503.

[50] Q. Dai, T.Y. Tang, Q.Q. Liang, Z.Q. Chen, Y. Wang, Y.L. Tang, Exploration of A_2BH_6 (A= K, Rb; B= Ge, Sn) hydrides for hydrogen storage applications: a first principles study, Int. J. Hydrogen Energy 92 (2024) 769–778.

[51] C.J. Bartel, C. Sutton, B.R. Goldsmith, R. Ouyang, C.B. Musgrave, L.M. Ghiringhelli, M. Scheffler, New tolerance factor to predict the stability of perovskite oxides and halides, Sci. Adv. 5 (2) (2019) eaav0693.

[52] A. Gencer, G. Surucu, Investigation of structural, electronic and lattice dynamical properties of $XNiH_3$ (X= Li, Na and K) perovskite type hydrides and their hydrogen storage applications, Int. J. Hydrogen Energy 44 (29) (2019) 15173–15182.

[53] A. Schneemann, J.L. White, S. Kang, S. Jeong, L.F. Wan, E.S. Cho, V. Stavila, Nanostructured metal hydrides for hydrogen storage, Chem. Rev. 118 (22) (2018) 10775–10839.

[54] G.M. Mustafa, B. Younas, H.D. Alkhaldi, A. Mera, A.K. Alqorashi, J. Hakami, S. A. Mahmoud, I. Boukhris, Q. Mahmood, First principle study of physical aspects and hydrogen storage capacity of magnesium-based double perovskite hydrides Mg_2XH_6 (X = Cr, Mn), Int. J. Hydrogen Energy 95 (2024) 300–308.

[55] N. Xu, R. Song, S. Chen, Y. Chen, S. Li, Z. Jiang, W. Zhang, First-principles study on the structure, mechanical, electrical, optical, kinetic, thermodynamic and hydrogen storage properties of the hydride perovskites $XScH_3$ (X= K, Rb, Cs) for hydrogen storage applications, J. Energy Storage 107 (2025) 114945.

[56] Ç. Yamçıçıer, C. Kürkçü, Investigation of structural, electronic, elastic, vibrational, thermodynamic, and optical properties of Mg_2NiH_4 and Mg_2RuH_4 compounds used in hydrogen storage, J. Energy Storage 84 (2024) 110883.

[57] A. Manzoor, M.A. Ullah, M.W. Yasin, S.S.A. Gillani, M. Ikram, M. Rizwan, Investigation of $SrLiF_{3-x}H_x$ perovskites through ion replacement mechanism for advanced solid hydrogen storage systems: a prediction through DFT-based calculations, J. Energy Storage 88 (2024) 111639.

[58] Q. Ain, H.T. Naeem, M. Ali, J. Munir, Z. Bibi, H.M. Ghaithan, S.M. Qaid, A precise prediction of structure stability and hydrogen storage capability of $KCdH_3$ perovskite hydride using density functional theory calculations, J. Energy Storage 100 (2024) 113734.

[59] M. Ali, Q. Ain, M. Alkadi, J. Munir, Z. Bibi, M.W. Younis, S.M. Qaid, First-principles evaluation of $LiCaF_{3-\alpha}H_\alpha$ as an effective material for solid-state hydrogen storage, J. Energy Storage 83 (2024) 110731.

[60] C. Kittel, P. McEuen, Introduction to Solid State Physics, John Wiley & Sons, 2018.

[61] S. Al, N. Cavdar, N. Arikan, Computational evaluation of comprehensive properties of MgX_3H_8 (X= Sc, Ti and Zr) as effective solid-state hydrogen storage materials, J. Energy Storage 80 (2024) 110402.

[62] G. Surucu, A. Gencer, A. Candan, H.H. Gullu, M. Isik, $CaXH_3$ (X= Mn, Fe, Co) perovskite-type hydrides for hydrogen storage applications, Int. J. Energy Res. 44 (3) (2020) 2345–2354.

[63] G. Surucu, A. Candan, A. Gencer, M. Isik, First-principles investigation for the hydrogen storage properties of $NaXH_3$ (X= Mn, Fe, Co) perovskite-type hydrides, Int. J. Hydrogen Energy 44 (57) (2019) 30218–30225.

[64] F. Mouhat, F.-X. Coudert, Necessary and sufficient elastic stability conditions in various crystal systems, Phys. Rev. B 90 (2014) 224104.

[65] M. Born, On the stability of crystal lattices. I, Math. Proc. Camb. Philos. Soc. 36 (1940) 160–172.

[66] S. Bahhar, A. Tahiri, A. Jabar, M. Louzazni, M. Idiri, H. Bioud, Computational assessment of $MgXH_3$ (X= Al, Sc and Zr) hydrides materials for hydrogen storage applications, Int. J. Hydrogen Energy 58 (2024) 259–267.

[67] W. Voigt, Lehrbuch der Kristallphysik (Textbook of Crystal Physics), BG Teubner, Leipzig und Berlin, 1928.

[68] A. Reuß, Berechnung der Fließgrenze von Mischkristallen auf Grund der Plastizitätsbedingung für Einkristalle, ZAMM - J. Appl. Math. Mech. 9 (1) (1929) 49–58.

[69] R. Hill, The elastic behaviour of a crystalline aggregate, Proc. Phys. Soc. A 65 (1952) 349.

[70] W. Khan, Computational screening of $BeXH_3$ (X: Al, Ga, and In) for optoelectronics and hydrogen storage applications, Mater. Sci. Semicond. Process. 174 (2024) 108221.

[71] H. Murtaza, Q. Ul Ain, J. Munir, H.M. Ghaithan, A.A.A. Ahmed, S.M. Qaid, Exploring the optoelectronic attributes, thermoelectric and photocatalytic potential of double perovskites $Cs_2BB'H_6$ (B= Al, Na and B′= Tl, In): a DFT study, Mater. Sci. Eng. B 301 (2024) 117171.
[72] S.F. Pugh, Relations between the elastic moduli and the plastic properties of polycrystalline pure metals, Philos. Mag. J. Sci. 45 (1954) 823–843.
[73] S. Menakh, B. Daoudi, A. Boukraa, K. Ferkous, First-principles calculations to investigate structural, elastic, electronic and optical properties of A_2OsH_6 for storage hydrogen and optoelectronic devices, Comput. Condens. Matter 31 (2022) e00684.
[74] H. Ziani, A. Gueddim, N. Bouarissa, L. Gacem, Ab initio studies of A_2PtH_6 (A= K, Rb) materials for hydrogen storage purposes and optoelectronic applications, Mater. Sci. Eng. B 269 (2021) 115154.
[75] E. Schreiber, O.L. Anderson, S. Naohiro, Elastic Constants and Their Measurement, McGraw-Hill, New York, 1973.
[76] P. Ravindran, L. Fast, P.A. Korzhavyi, B. Johansson, J. Wills, O. Eriksson, Density functional theory for calculation of elastic properties of orthorhombic crystals: application to $TiSi_2$, J. Appl. Phys. 84 (1998) 4891–4904.
[77] A.I. Bashir, et al., Density-functional quantum computations on bandgap engineering and tuning of optoelectronic properties of MgH_2 via Mo doping: prospects and potential for clean energy hydrogen-storage fuel and optoelectronic applications, Int. J. Hydrogen Energy 48 (53) (2023) 20419–20429.
[78] C. Zhou, A Study of Advanced Magnesium-Based Hydride and Development of a Metal Hydride Thermal Battery System, The University of Utah, 2015.
[79] R.K. Pingak, et al., A DFT investigation of lead-free $TlSnX_3$ (X= Cl, Br, or I) perovskites for potential applications in solar cells and thermoelectric devices, RSC Adv. 13 (48) (2023) 33875–33886.
[80] P. Prelovs, Temperature and doping dependence of the high-energy kink in cuprates, Phys. Rev. Lett. 100 (2008) 036402.
[81] İ.K. Durukan, Y.O. Ciftci, H. Tekin, A new candidate for optoelectronic device applications: CoTiX (X: P, As, Sb) half-Heusler compounds, Physica B 678 (2024) 415752.
[82] P.S.M.J. Spoor, Phys. Rev. Lett. 75 (19) (1995) 3462–3465.
[83] S.I. Ranganathan, M. Ostoja-Starzewski, Universal elastic anisotropy index, Phys. Rev. Lett. 101 (2008) 055504.
[84] C.M. Kube, Elastic anisotropy of crystals, AIP Adv. 6 (2016) 095209.
[85] M.K. Samal, A. Syed, J. Chattopadhyay, A.M. Ram, B. Paul, M.C. Reddy, Effect of texture on crack initiation toughness and the corresponding anisotropy in ductile fracture resistance of thin Zircaloy-4 sheets of Indian PHWR core component, J. Nucl. Mater. 535 (2020) 152189.
[86] N. Dalton, Approximate calculation of electronic band structures. IV. Density of states for transition metals, J. Phys. C Solid State Phys. 3 (9) (1970) 1912.
[87] A. Candan, A.K. Kushwaha, A first-principles study of the structural, electronic, optical, and vibrational properties for paramagnetic half-Heusler compound TiIrBi by GGA and GGA+ mBJ functional, Mater. Today Commun. 27 (2021) 102246.
[88] M.U. Ghani, et al., CASTEP investigation of structural, electronic, and optical properties of halide perovskites $RbXCl_3$ (X= Ge, Sn, Pb) for solar cell applications, Inorg. Chem. Commun. 155 (2023) 111007.
[89] J. Nan, X. Guo, J. Xiao, X. Li, W. Chen, W. Wu, et al., Nanoengineering of 2D MXene-based materials for energy storage applications, Small 17 (9) (2021) 1902085.
[90] M.A. Morsi, G.M. Asnag, A.S. Assran, R. Alwafi, A.E. Tarabiah, N.A. Alshehri, et al., Reinforced PEO/Cs polymer blends with Al_2O_3/TiO_2 hybrid nanofillers: nanocomposites for optoelectronics and energy storage, J. Energy Storage 88 (2024) 111554.
[91] A. Obeidat, A. Alrousan, S. Abu-Rajouh, First-principles study of structural, hydrogen storage, mechanical, electronic, and optical properties of K_2NaXH_6 (X = Al, As, Bi, Ga, In) double perovskite hydrides, J. Power Sources 642 (2025) 236944.
[92] T.O. Magu, O.R. Jolayemi, E. Emmanuel, R. Musa, S.S. Ikiensikimama, Implication of group 13 elements for the tailoring of Fe_3H hydride perovskites for optoelectronic and hydrogen storage applications: an intuition from theoretical study, J. Phys. Chem. Solid 199 (2025) 112544.
[93] T. Tang, Y. Tang, Computational investigation of comprehensive properties of AlX_3H_9 (X = Ca, Sc, Zr) materials for high-performance hydrogen storage, J. Energy Storage 108 (2025) 115102.
[94] S. Al-Qaisi, N. Iram, N. Sfina, A. Boutramine, H.R. Jappor, A.H. Alfaifi, G. Murtaza, Comprehensive DFT study of K_2TlZI_6 (Z = Al, In) double perovskites: structural stability and potential for optoelectronic and thermoelectric energy harvesting, Phys. B Condens. Matter 710 (2025) 417239.
[95] T. Tang, Y. Tang, First-principles calculations to investigate Mg_3XH_8 (X = Ca, Sc, Ti, V, Cr, Mn) materials for hydrogen storage, Int. J. Hydrogen Energy 74 (2024) 372–383.
[96] D.W. Boukhvalov, et al., Thermal effects and halide mixing of hybrid perovskites: MD and XPS studies, J. Phys. Chem. C 124 (2019) 135–140.
[97] Z. Li, et al., Enhanced Li-ion battery performance based on multisite oxygen vacancies in WO_{3-x}@rGO negative electrode, Chem. Eng. J. 498 (2024) 155383.